

Diffeomorphic Deformation via Sliced Wasserstein Distance Optimization for Cortical Surface Reconstruction

Tung Le* Khai Nguyen[◇] Shanlin Sun* Kun Han* Nhat Ho[◇] Xiaohui Xie*

*University of California, Irvine

[◇]The University of Texas at Austin

May 30, 2023

Abstract

Mesh deformation is a core task for 3D mesh reconstruction, but defining an efficient discrepancy between predicted and target meshes remains an open problem. A prevalent approach in current deep learning is the set-based approach which measures the discrepancy between two surfaces by comparing two randomly sampled point-clouds from the two meshes with Chamfer pseudo-distance. Nevertheless, the set-based approach still has limitations such as lacking a theoretical guarantee for choosing the number of points in sampled point-clouds, and the pseudo-metricity and the quadratic complexity of the Chamfer divergence. To address these issues, we propose a novel metric for learning mesh deformation. The metric is defined by sliced Wasserstein distance on meshes represented as probability measures that generalize the set-based approach. By leveraging probability measure space, we gain flexibility in encoding meshes using diverse forms of probability measures, such as continuous, empirical, and discrete measures via *varifold* representation. After having encoded probability measures, we can compare meshes by using the sliced Wasserstein distance which is an effective optimal transport distance with linear computational complexity and can provide a fast statistical rate for approximating the surface of meshes. Furthermore, we employ a neural ordinary differential equation (ODE) to deform the input surface into the target shape by modeling the trajectories of the points on the surface. Our experiments on cortical surface reconstruction demonstrate that our approach surpasses other competing methods in multiple datasets and metrics.

1 Introduction

Mesh deformation is a fundamental task in 3D computer vision and computer graphics. A wide range of shape reconstruction tasks [15, 35, 49, 55, 57, 58, 77] and shape registration [5, 20, 7, 39, 21, 6, 66, 31] leverages state-of-the-art mesh deformation methodology. One popular approach for mesh deformation is to estimate the vertex displacement vectors (3D offsets) while keeping their connectivity [74, 10]. However, displacement-based methods cannot guarantee the manifoldness of the resulting mesh and often produce self-intersecting faces. To address this issue, diffeomorphic transformation [62, 4] is one effective way to deform a mesh while preserving its topology. As an instance of diffeomorphic surface deformation, Neural Mesh Flow (NMF) [30] learns a sequence of diffeomorphic flows between two meshes and models the trajectories of the mesh vertices as ordinary differential equations (ODEs). However, these methods have limited shape representation capacity and struggle to perform well on complex manifolds. To overcome this limitation, several diffeomorphic mesh deformation models have

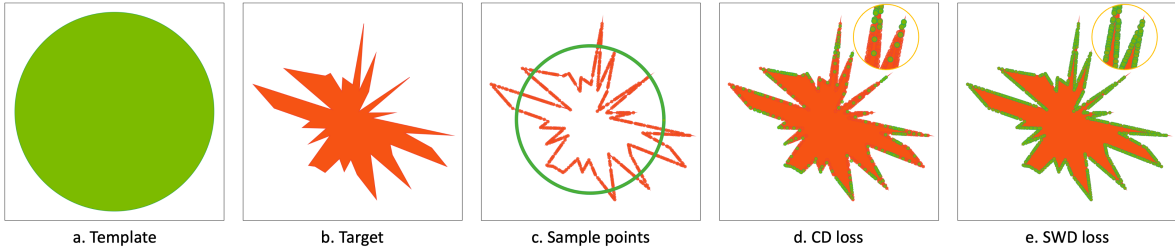


Figure 1: **2D deformation toy example.** We deform a (a) template circle to a (b) target polygon via an optimization-based setting. (c) Points are uniformly sampled from the two contours. CD loss is easily trapped at local minima, i.e. the green points are not uniformly distributed on the target contour as desired. In contrast, (e) SWD loss can find the optimal transport plan among discrete probability measures, i.e. the resulting points are distributed more uniformly along the contour. More details about this toy example can be found in the Appendix A.

been proposed, such as CortexODE [44] and CorticalFlow [41], which aim to handle hard manifolds, such as the cortical surface. While CorticalFlow [41] introduces diffeomorphic mesh deformation (DMD) modules to learn a series of stationary velocity fields, CortexODE [44] encodes spatial information of the MRI images along with vertices features using an MLP model and employs neural ODEs [14] to model the trajectories of the points. Nonetheless, these approaches often rely on Chamfer distance as the objective function, which might have disadvantages.

Selecting an appropriate metric to evaluate the dissimilarity between two meshes is a crucial step in learning deformation mesh models. Recent literature favors the approach of using set-based comparison due to its simplicity. In particular, the set-based approach first samples two sets of points on the surface meshes, and then use Chamfer distance (CD) [22, 23, 29] to compare two meshes and optimize them. However, the CD loss tends to get trapped in local minima easily [1, 54, 53], failing to distinguish bad samples from the true ones, as demonstrated by our toy example in Fig. 1. Although a weighted CD has been proposed to prioritize fitting local regions with high curvatures in Vox2Cortex [10], the issue is only alleviated but not resolved completely, still resulting in suboptimal assignments between two sets of points. Therefore, we propose novel approaches to transform a mesh into a probability measure that generalizes the set-based approach. Furthermore, by relying on the probability measure approach, we can employ geometric measure theory to represent mesh as an oriented varifold [2, 68, 26] and get a better approximation of the mesh compared to the random sampling approach. After that, we adopt efficient optimal transport to compare these measures since optimal transport distances are naturally fitted to compare disjoint-supports measures.

Wasserstein distance [59, 70] has been widely recognized as an effective optimal transport metric to compare two probability measures, especially when their supports are disjointed. Despite having a lot of appealing properties, the Wasserstein distance has high computational complexity. In particular, when dealing with discrete probability measures that have at most m supports, the time and memory complexities of the Wasserstein distance are $\mathcal{O}(m^3 \log m)$ and $\mathcal{O}(m^2)$, respectively. The issue becomes more problematic when the Wasserstein distance

is computed on different pairs of measures as in mesh applications, namely, each mesh can be treated as a probability measure.

To improve the computational complexities of the Wasserstein distance, by adding entropic regularization and using the Sinkhorn algorithm [19], an ϵ -approximation of Wasserstein distance can be obtained in $\mathcal{O}(m^2/\epsilon^2)$. However, this approach cannot reduce the memory complexity of $\mathcal{O}(m^2)$ due to the storage of the cost matrix. Moreover, the entropic regularization approach cannot lead to a valid metric between probability measures since the resulting discrepancy does not satisfy the triangle inequality. A more efficient approach based on the closed-form solution of Wasserstein is sliced Wasserstein distance (SWD) [11], which is computed as the expectation of the Wasserstein distance between random one-dimensional push-forward measures from two original measures. SWD can be solved in $\mathcal{O}(m \log m)$ time complexity while having a linear memory complexity $\mathcal{O}(m)$.

In this paper, we propose a learning-based diffeomorphic deformation framework via sliced Wasserstein distance optimization, dubbed DD-SWD, that learns continuous dynamics to smoothly deform an initial mesh towards an intricate shape based on volumetric input. Specifically, given a 3D brain MRI volume, we aim to reconstruct the highly folded white matter surface region. We first extract the initial surface from the white matter segmentation mask of the brain MRI image, then we deform the initial surface to the target surface by modeling its vertices trajectory via neural ODE [14]. Our deformation model is optimized via sliced Wasserstein distance loss by encoding the mesh as a probability measure. We further represent mesh as an oriented varifold and empirically show that our approach surpasses other related works on multiple datasets and metrics, namely, almost self-intersection-free while maintaining high geometric accuracy. It is worth noting that although our DD-SWD is developed within the scope of cortical surface reconstruction, the underlying concepts can be extended to other 3D deformation networks.

Contribution. In summary, our contributions are two-fold:

1. We propose a new metric for learning mesh deformation. Our metric utilizes the sliced Wasserstein distance (SWD), which operates on meshes represented as probability measures. By relying on probability measure space, we can encode a mesh as three forms of probability measures including a continuous probability measure, an empirical probability measure, and a discrete probability measure via an oriented varifold. Additionally, we demonstrate that sliced Wasserstein distance (SWD) is a valid computationally fast metric between probability measures and provide the approximation bound between the SWD between empirical probability measures and the SWD between continuous probability measures. To the best of our knowledge, we are the first to adopt SWD as an efficient metric in optimizing meshes in learning-based diffeomorphic deformation models.
2. We conduct extensive experiments on white matter reconstruction by employing neural ODE [14] to deform the initial surface to the target surface. Our experiments on multiple brain datasets demonstrate that our method surpasses existing state-of-the-art related works in terms of geometric accuracy, self-intersection ratio, and consistency.

Notations. For any $d \geq 2$, we denote $\mathbb{S}^{d-1} := \{\theta \in \mathbb{R}^d \mid \|\theta\|_2^2 = 1\}$ and $\mathcal{U}(\mathbb{S}^{d-1})$ as the unit hyper-sphere and its corresponding uniform distribution. We denote $\theta\#\mu$ as the push-forward

measures of μ through the function $f: \mathbb{R}^d \rightarrow \mathbb{R}$ that is $f(x) = \theta^\top x$. Furthermore, we denote δ_x as Dirac distribution at a location x , and $\mathcal{P}_p(\mathbb{R}^d)$ is the set of probability measures over \mathbb{R}^d that has finite p -moment. By abuse of notations, we use capitalized letters for both random variables and sets.

2 Background

In this section, we first review the set-based approach for comparing two meshes. After that, we review the definition of Wasserstein distance and diffeomorphic flows for deforming meshes.

2.1 The Set-Based Approach: Mesh to Point-cloud

Mesh to a point-cloud. To sample a point p from a mesh, a face $f = (x_1, x_2, x_3)$ is first sampled with the probability proportional to the area of the face. Then, the position p can be sampled by setting $p := w_1x_1 + w_2x_2 + w_3x_3$, where $w_1 + w_2 + w_3 = 1$ are random barycentric coordinates which are uniformly distributed over a triangle [60, 74]. The process is repeated until getting the desired number of points.

Comparing two point-clouds. After having representative point-clouds from meshes, a discrepancy in the space of point-clouds (sets) is used. The most widely used discrepancy for point-cloud is the set-based Chamfer pseudo distance [8]. For any two point-clouds X and Y , the Chamfer distance is:

$$\text{CD}(X, Y) = \frac{1}{|X|} \sum_{x \in X} \min_{y \in Y} \|x - y\|_2^2 + \frac{1}{|Y|} \sum_{y \in Y} \min_{x \in X} \|x - y\|_2^2, \quad (1)$$

where $|X|$ denotes the number of points in X .

2.2 Wasserstein distance

We now review the definition of the Wasserstein distance for comparing two probability measures $\mu \in \mathcal{P}_p(\mathbb{R}^d)$ and $\nu \in \mathcal{P}_p(\mathbb{R}^d)$. The Wasserstein- p [69] distance between μ and ν as follows:

$$W_p^p(\mu, \nu) := \inf_{\pi \in \Pi(\mu, \nu)} \int_{\mathbb{R}^d \times \mathbb{R}^d} \|x - y\|_p^p d\pi(x, y), \quad (2)$$

where $\Pi(\mu, \nu)$ is the set of joint distributions that have marginals are μ and ν respectively. A benefit of Wasserstein distance is that it can handle two measures that have disjointed supports.

Wasserstein distance between continuous measures. Computing the Wasserstein distance accurately between continuous measures is still an open question [38] due to the non-optimality and instability of the minimax optimization for continuous functions which are the Kantorovich potentials [3]. Hence, discrete representations of the continuous measures are often used as proxies to compare them. i.e., the plug-in estimator [9]. In particular, let $X_1, \dots, X_m \stackrel{i.i.d}{\sim} \mu$ and $Y_1, \dots, Y_m \stackrel{i.i.d}{\sim} \nu$, the Wasserstein distance $W_p(\mu, \nu)$ is approximated by $W_p(\hat{\mu}_m, \hat{\nu}_m)$ with $\hat{\mu}_m = \frac{1}{m} \sum_{i=1}^m \delta_{X_i}$ and $\hat{\nu}_m = \frac{1}{m} \sum_{i=1}^m \delta_{Y_i}$ are the corresponding empirical measures. However,

we have the convergence rate of the Wasserstein distance is $\mathcal{O}(m^{-1/d})$ [48]. Namely, we have $\mathbb{E}[|W_p(\hat{\mu}_m, \hat{\nu}_m) - W_p(\mu, \nu)|] \leq Cn^{-1/d}$ for an universal constant C , where $\hat{\mu}_m = \frac{1}{m} \sum_{i=1}^m \delta_{X_i}$ is the corresponding empirical measure. Therefore, the Wasserstein distance suffers from the curse of dimensionality i.e., the Wasserstein distance needs more samples to represent the true measure well when dealing with high-dimensional measures. In the setting of comparing meshes, the Wasserstein distance will be worse if we use more features for meshes e.g., normals, colors, and so on.

Wasserstein distance between discrete measures. When μ and ν are two discrete probability measures that have at most m supports, the time complexity and memory complexity to compute the Wasserstein distance are $\mathcal{O}(m^3 \log m)$ and $\mathcal{O}(m^2)$ respectively. Therefore, using the plug-in estimator requires expensive computation since it requires a relative large value of m to the dimension.

2.3 Diffeomorphic Flows

Diffeomorphic flows can be established by dense point correspondences between source and target surfaces. Given an input surface, the trajectories of the points can be modeled by an ODE, where the derivatives of the points are parameterized by a deep neural network (DNN). Specifically, let $\Phi(\mathbf{p}, t) : \Omega \subset \mathbb{R}^3 \times [0, 1] \mapsto \Omega \subset \mathbb{R}^3$ be a continuous hidden state of the neural network that defines a trajectory from source position $\mathbf{p} = \Phi(\mathbf{p}, 0)$ to the target position $\mathbf{p}' = \Phi(\mathbf{p}, 1)$, and \mathbb{F}_ϕ be a DNN with parameters ϕ . An ordinary differential equation (ODE) with the initial condition is defined as:

$$\frac{\partial \Phi(\mathbf{p}, t)}{\partial t} = \mathbb{F}_\phi(\Phi(\mathbf{p}, t), t) \quad \text{s.t.} \quad \Phi(\mathbf{p}, 0) = \mathbf{p}, \quad (3)$$

If \mathbb{F}_ϕ is Lipschitz, a solution to Eq. 3 exists and is unique in the interval $[0, 1]$, which provides a theoretical guarantee that any two deformation trajectories do not intersect with each other [17].

3 Diffeomorphic Deformation via Sliced Wasserstein Distance Optimization

In this section, we generalize the set-based mesh representation by discussing three ways of transforming mesh into probability measure encoding. We further employ sliced Wasserstein distance as an objective function in the diffeomorphic flow model for cortical surface reconstruction task.

3.1 The Measure-Approach: Mesh to Probability Measure

We now discuss the approach that we rely on to compare meshes via probability metrics. In particular, we consider transforming a mesh into a probability measure.

Mesh to a continuous and hierarchical probability measure. Let a mesh \mathcal{M} has a set of faces $F^\mathcal{M} = \{f_1^\mathcal{M}, \dots, f_N^\mathcal{M}\}$ ($N > 0$) where a face f is represented by its vertices $\text{Ver}(f) = \{x_1, \dots, x_{v^f}\}$ ($v^f \geq 3$). We now can define a probability measure over faces, namely, $\mu^\mathcal{M}(f) = \sum_{i=1}^N \frac{\text{Vol}(f_i)}{\sum_{j=1}^N \text{Vol}(f_j^\mathcal{M})} \delta_{f_i^\mathcal{M}}$ is the categorical distribution over the faces that

has the weights proportional to the areas of the faces (volume of the convex hull of vertices). For example, in the case of triangle meshes, we have $\text{Ver}(f) = (x_1, x_2, x_3)$ and $\text{Vol}(f) = \frac{1}{2} \|(x_2 - x_1) \times (x_3 - x_1)\|$. Given a face f , the conditional distribution for a point in the space is $\mu^{\mathcal{M}}(x|f) = \frac{1}{\text{Vol}(f)}, \forall x \in \text{ConvexHull}(\text{Ver}(f))$. Therefore, the marginal distribution for a point in the space induced by a mesh \mathcal{M} is $\mu^{\mathcal{M}}(x) = \sum_{i=1}^N \mu^{\mathcal{M}}(x|f_i^{\mathcal{M}}) \mu^{\mathcal{M}}(f_i^{\mathcal{M}})$. It is worth noting that given two meshes \mathcal{M}_1 and \mathcal{M}_2 , their corresponding probability measures $\mu^{\mathcal{M}_1}$ and $\mu^{\mathcal{M}_2}$ are likely to have disjoint supports. Therefore, the optimal transport distances are natural metrics for comparing them.

Mesh to an empirical probability measure. As discussed in the background, the most computationally efficient and stable approach to approximate the Wasserstein distance is through the plugin estimator [9]. In particular, let x_1, \dots, x_m be a set of points that are independently identically sampled from $\mu^{\mathcal{M}_1}$ and y_1, \dots, y_m be a set of points that are independently identically sampled from $\mu^{\mathcal{M}_2}$. After that, we can define $\hat{\mu}_m^{\mathcal{M}_1} = \frac{1}{m} \sum_{i=1}^m \delta_{x_i}$ and $\hat{\mu}_m^{\mathcal{M}_2} = \frac{1}{m} \sum_{i=1}^m \delta_{y_i}$ as the represented empirical probability measure of the two meshes \mathcal{M}_1 and \mathcal{M}_2 respectively. Finally, the discrete Wasserstein distance is computed between $\hat{\mu}_m^{\mathcal{M}_1}$ and $\hat{\mu}_m^{\mathcal{M}_2}$ as the final discrepancy.

Mesh to a discrete probability measure. To have a richer representation of mesh, we consider the discrete probability measure representation through varifold. Let M be a smooth submanifold of dimension 2 embedded in the ambient space of \mathbb{R}^n , e.g. $n = 3$ for surface, with finite total volume $\text{Vol}(M) < \infty$. For every point $p \in M$, there exists a tangent space $T_p M$ be a linear subspace of \mathbb{R}^n . To establish an orientation of M , it is essential to orient the tangent space $T_p M$ for every $p \in M$. This ensures that each oriented tangent space can be represented as an element of an oriented Grassmannian. Inspired from previous works [27, 68, 13, 36], M can be associated as an oriented varifold $\tilde{\mu}^M$, i.e. a distribution on the position space and tangent space orientation $\mathbb{R}^n \times \mathbb{S}^{n-1}$, as follows: $\tilde{\mu}^M = \int_M \delta_{(p, \vec{n}(p))} d\text{Vol}(p)$, where $\vec{n}(p)$ is the unit oriented normal vector to the surface at p . Once established the oriented varifold for a smooth surface, an oriented varifold for triangular mesh \mathcal{M} that approximates smooth shape M can be derived as follows:

$$\tilde{\mu}^{\mathcal{M}} = \sum_{i=1}^{|F|} \tilde{\mu}^{f_i} = \sum_{i=1}^{|F|} \int_{f_i} \delta_{(p_i, \vec{n}(p_i))} d\text{Vol}(p) \approx \sum_{i=1}^{|F|} \alpha_i \delta_{(p_i, \vec{n}(p_i))}, \quad (4)$$

where p_i is the barycenter of the vertices of face f_i and $\alpha_i := \text{Vol}(f_i)$ is the area of the triangle. To ensure that $\tilde{\mu}^{\mathcal{M}}$ possesses the characteristic of a discrete measure, we normalize α_i 's such that they sum up to 1. It is worth noting that provided the area of triangular is sufficiently small, $\tilde{\mu}^{\mathcal{M}}$ gives an acceptable approximation of the discrete mesh \mathcal{M} in terms of oriented varifold [36].

3.2 Effective and Efficient Mesh Comparison with Sliced Wasserstein

Sliced Wasserstein distance. The sliced Wasserstein distance [11] (SWD) between two probability measures $\mu \in \mathcal{P}_p(\mathbb{R}^d)$ and $\nu \in \mathcal{P}_p(\mathbb{R}^d)$ is defined as:

$$\text{SW}_p^p(\mu, \nu) = \mathbb{E}_{\theta \sim \mathcal{U}(\mathbb{S}^{d-1})} [\text{W}_p^p(\theta \# \mu, \theta \# \nu)], \quad (5)$$

The benefit of SW is that $W_p^p(\theta_{\sharp}^{\mu}, \theta_{\sharp}^{\nu})$ has a closed-form solution which is $\int_0^1 |F_{\theta_{\sharp}^{\mu}}^{-1}(z) - F_{\theta_{\sharp}^{\nu}}^{-1}(z)|^p dz$ with F^{-1} denotes the inverse CDF function. The expectation is often approximated by Monte Carlo sampling, namely, it is replaced by the average from $\theta_1, \dots, \theta_L$ (L is the number of projections) that are drawn i.i.d from $\mathcal{U}(\mathbb{S}^{d-1})$. In particular, we have:

$$\widehat{SW}_p^p(\mu, \nu) = \frac{1}{L} \sum_{l=1}^L W_p^p(\theta_l^{\sharp} \mu, \theta_l^{\sharp} \nu). \quad (6)$$

The computational complexity and memory complexity of the Monte Carlo estimation of SW are $\mathcal{O}(Lm \log m)$ and $\mathcal{O}(Lm)$ [50] respectively when μ and ν are discrete measures with at most m supports. Therefore, the sliced Wasserstein is naturally suitable for large-scale mesh comparison.

Convergence rate. We now discuss the non-asymptotic convergence of the Monte Carlo estimation of the sliced Wasserstein between two empirical probability measures to the sliced Wasserstein between the corresponding two continuous probability measures on surface meshes.

Theorem 1. *For any two meshes \mathcal{M}_1 and \mathcal{M}_2 , let $X_1, \dots, X_m \stackrel{i.i.d}{\sim} \mu^{\mathcal{M}_1}(x)$, $Y_1, \dots, Y_m \stackrel{i.i.d}{\sim} \mu^{\mathcal{M}_2}(x)$, $\hat{\mu}_m^{\mathcal{M}_1}(x) = \frac{1}{m} \sum_{i=1}^m \delta_{X_i}$ and $\hat{\mu}_m^{\mathcal{M}_2}(x) = \frac{1}{m} \sum_{i=1}^m \delta_{Y_i}$ be the corresponding empirical distribution. Assume that $\mu^{\mathcal{M}_1}$ and $\mu^{\mathcal{M}_2}$ have compact supports with the diameters are at most R , we have the following approximation error :*

$$\begin{aligned} \mathbb{E} \left[\left| \widehat{SW}_p^p(\hat{\mu}_m^{\mathcal{M}_1}, \hat{\mu}_m^{\mathcal{M}_2}; L) - SW_p^p(\mu^{\mathcal{M}_1}, \mu^{\mathcal{M}_2}) \right| \right] &\leq RC_{p,R} \sqrt{\frac{(d+1) \log m}{m}} \\ &+ \frac{1}{\sqrt{L}} \mathbb{E} \left[\text{Var} [W_p^p(\theta_{\sharp}^{\hat{\mu}_m^{\mathcal{M}_1}}, \theta_{\sharp}^{\hat{\mu}_m^{\mathcal{M}_2}})]^{1/2} | X_{1:m}, Y_{1:m} \right], \end{aligned}$$

for an universal constant $C_{p,R} > 0$. The variance is with respect to $\theta \sim \mathcal{U}(\mathbb{S}^{d-1})$.

Theorem 1 suggests that when using empirical probability measure to approximate meshes, the error between the Monte Carlo estimation of sliced Wasserstein distance between empirical distributions over two sampled point-clouds and sliced Wasserstein distance between two continuous distributions on meshes surface is bounded by the rate of $m^{-1/2}$ and $L^{-1/2}$. It means that, when increasing the number of points and the number of projections, the error reduces by the square root of them. This rate is very fast since it does not depend exponentially on the dimension, hence, it is scalable to meshes with high-dimensional features at vertices, such as normals, colors, and so on. Leveraging the scaling property and the approximation of varifold to mesh \mathcal{M} mentioned in Sec 3.1, we can represent meshes as discrete measures $\tilde{\mu}^{\mathcal{M}}$ and optimize $\widehat{SW}_p^p(\tilde{\mu}^{\mathcal{M}_1}, \tilde{\mu}^{\mathcal{M}_2}; L)$ as the objective function. The proof of Theorem 1 is given in Appendix B. It is worth noting that a similar property is not able to be derived for Chamfer since it is a discrepancy on sets that cannot be generalized to compare meshes.

3.3 Sliced Wasserstein Diffeomorphic Flow for Cortical Surface Reconstruction

Diffeomorphic deformation framework for reconstructing cortical surfaces. In this section, we present DD-SWD that incorporates diffeomorphic deformation and sliced

Wasserstein distance to reconstruct the cortical surface. Specifically, our goal is to derive a high-resolution, 2D manifold of the white matter that is topologically accurate from a 3D brain MR image. Let $\mathbf{I} \in \mathbb{R}^{D \times W \times H}$ be a MRI volume and $\mathcal{M} = (\mathcal{V}, \mathcal{F})$ be a 3D triangle mesh. The corresponding vertices of the mesh are represented by $v \in \mathbb{R}^3$. Firstly, we train a U-Net model to automatically predict the white matter segmentation mask from \mathbf{I} . Then, a signed distance function (SDF) is extracted from the binary mask before employing Marching Cubes [42] to get the initial surface. After getting the initial surface \mathcal{M}_0 , the trajectory of each coordinate v_0 is modeled via the ODE with initial condition from Eq. 3. Inspired from [45, 44], we concatenate the point features with the corresponding cube features sampling from \mathbf{I} as a new feature vector. The new feature is passed through a multilayer perceptron \mathbb{F}_ϕ to learn the deformation. More implementation settings are included in the Appendix C.

Sliced Wasserstein distance as a loss function. To train the DD-SWD model, we minimize the distance between predicted mesh $\hat{\mathcal{M}}$ and the ground truth mesh \mathcal{M}^* . We adopt a novel way of transforming mesh into a probability measure and leveraging sliced Wasserstein distance (SWD) as a loss function to optimize two discrete meshes. As discussed, the SW is a valid metric on the space of distribution and can guarantee the convergence of the probability measure. Moreover, as shown in Theorem 1, the sample complexity of the SW is bounded with a parametric rate, hence, it is suitable to use the SW to compare empirical probability measures as the proxy for the continuous mesh probability measure. Therefore, we sample points on $\hat{\mathcal{M}}$ and \mathcal{M}^* as probability measures and compute SWD loss between these two measures without regularization terms. Additionally, we can represent mesh as discrete probability measures, i.e. oriented varifold, and utilize the same objective function. Based on our observations, the varifold representation has shown better performance compared to encoding using empirical probability measures, which we provide a more detailed comparison in our ablation study in Sec. 5.3. As a result, we assume that our experiments in the following sections will be conducted using the oriented varifold approach unless otherwise specified.

4 Related Works

Deformation network for surface reconstruction. 3D surface reconstruction can be obtained from various approaches such as volumetric, implicit surfaces, and geometric deep learning methods. While volumetric-based [16, 32, 67, 73, 18] and implicit surface-based [49, 57, 76] methods can directly obtain surface by employing iso-surface extraction methods, such as Marching Cubes [42], they often require extensive post-processing to capture the high-quality resulting mesh. In contrast, geometric deep learning approaches use mesh deformation to achieve the target mesh while maintaining vertex connectivity [56, 65, 72, 75, 30, 10]. Among deformation-based approaches, diffeomorphic deformation demonstrates its capability to perform well on complex manifolds while keeping the ‘*manifoldness*’ property [30, 44, 40]. However, those methods often use Chamfer divergence as their objective optimization, which is sub-optimal, especially on intricate manifolds such as cortical surfaces, i.e. as illustrated in Fig. 2. Therefore, in this work, we address the problem by employing efficient optimal transport in optimizing mesh during training diffeomorphic deformation models.

Mesh as varifold representation. Varifolds were initially introduced in the realm of geometric measure theory as a practical approach to tackle Plateau’s problem [2], which

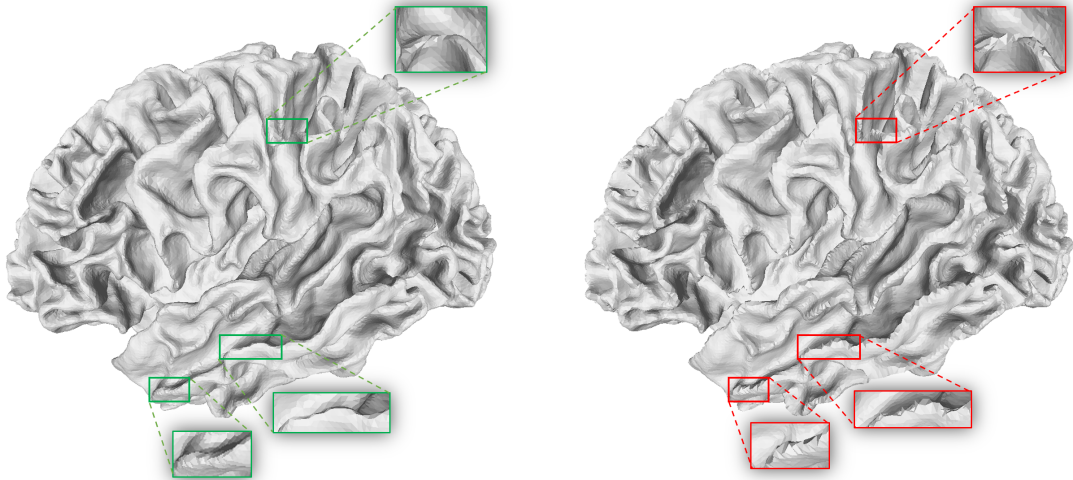


Figure 2: **Comparison between SWD loss (left) and CD loss (right).** The mesh obtained through probability measure representation and SWD optimization exhibits a more uniformly surfaced appearance compared to the set-based approach that optimizes with CD loss.

involves determining surfaces with a specified boundary that has the least area. Specifically, varifolds provide a convenient representation of geometric shapes, including rectifiable curves and surfaces, and serve as an effective geometric measure for optimization-based shape matching problems [13, 12, 36, 33, 61, 43]. In this work, we focus on employing varifold as a discrete measure approximating the mesh. To the best of our knowledge, we are the first to exploit oriented varifolds as discrete probability measures in the learning-based deformation framework.

5 Experiments

Within this section, we first provide detailed settings and conduct extensive experiments on multiple datasets. Furthermore, we also give a comprehensive ablation study to validate our findings.

5.1 Experimental Settings

Datasets. In order to assess how well our approach reconstructs cortical surfaces from MRI images, we employ three publicly available datasets: the Alzheimer’s Disease Neuroimaging Initiative (ADNI) dataset [34], the Open Access Series of Imaging Studies (OASIS) dataset [47], and the test-retest (TRT) dataset [46]. The pseudo-ground truth surfaces are obtained from Freesurfer v5.3 [25]. We strictly follow the pre-processing pipeline from [10]. Specifically, we first register the MRIs to the MNI152 scan. After padding the input images to have shape $192 \times 208 \times 192$, we resize them to $128 \times 144 \times 128$. The intensity values are min-max-normalized to the range $[0, 1]$. More details about the datasets are provided in our Appendix D.

Baselines. We train models for all competing methods using their official implementations and

recommended experimental settings. Then, we select the best checkpoints from the validation set to compare the performance. Specifically, we reproduce DeepCSR [18] in both the occupancy field and signed distance function (SDF) and report SDF results due to better performance. For Vox2Cortex [10], we use the authors’ suggestion with a high-resolution template with $\approx 168,000$ vertices for each structure to get the best performance. Finally, regarding CorticalFlow++ [63] and CortexODE [44], we retrain them with default settings.

Metrics. To evaluate the performance of our approach as well as other methods, we employ various metrics including earth mover’s distance (EMD), sliced Wasserstein distance (SWD), average symmetric surface distance (ASSD), Chamfer normals (CN), and self-intersection faces ratio (SI). We sample 100K points over the predicted and target surface to compute EMD, SWD, ASSD, and CN. Due to the large number of sampled points, we estimate EMD using entropic regularization and the Sinkhorn algorithm from [24]. Furthermore, we determine SI faces using PyMesh [78] library.

5.2 Results & Discussion

5.2.1 Quantitative Results

Geometric accuracy. As shown in Tab. 1, our DD-SWD provides more geometrically accurate surfaces than other competing methods in multiple metrics. Regarding optimal transport-based metrics, our method outperforms related works on SWD metrics in both datasets and only CortexODE [44] has a better EMD score than us at the right white matter reconstruction result. In terms of Chamfer divergence-based metrics, CortexODE [44] and CorticalFlow++ [63] are better than us in ASSD metric. However, we achieve better CN scores than CorticalFlow++ [63], and have a slightly comparable result with CortexODE [44].

Self-intersection. To evaluate the regularity of the resulting mesh, we report self-intersection faces (SI) in Tab. 1. Compare to GNN deformation-based methods such as Vox2Cortex [10] with no SI-free theoretical guarantee, diffeomorphic deformation-based methods such as CorticalFlow++ [63], CortexODE [44], and our proposed approach has much less SI. However, despite the nice property of existence and uniqueness of the solution of ODE models, CorticalFlow++ [63] and CortexODE [44] still introduce a certain amount of SI faces since they both rely on the optimization of Chamfer divergence on discretized vertices of the mesh. Our approach, on the other hand, represents mesh as probability measures and has strong theoretical optimization support by employing efficient optimal transport metric, thus can approximate the mesh much better with almost no SI faces, i.e. less than $10^{-4}\%$. DeepCSR [18] introduces no SI thanks to Marching Cubes [42] from the implicit surface but often has other artifacts and requires extensive topology correction.

Consistency. We compare the consistency of our DD-SWD, Vox2Cortex, CortexODE (which are all trained on OASIS), and FreeSurfer on the TRT dataset. We reconstruct white matter cortical surfaces from MRI images of the same subject on the same day and evaluated the EMD, SWD, and ASSD of the resulting reconstructions. The expectation is that the brain morphology of two consecutive scans taken on the same day should be similar to each other, except for the variations caused by the imaging process. To align pairs of images, we utilized the iterative closest-point algorithm (ICP) following [18]. As presented in Tab. 2, we outperform

Table 1: **Quantitative results of white matter surface reconstruction** in terms of earth mover’s distance (EMD), sliced Wasserstein distance (SWD), average symmetric surface distance (ASSD), Chamfer normals (CN), and self-intersection face ratio (SI) on ADNI and OASIS datasets. Best values are highlighted. EMD, SWD, ASSD results are in mm. All results are listed in the format “mean value \pm standard deviation”. **DD-SWD** represents the reconstruction results from our proposed approach. While \downarrow means smaller metric value is better, \uparrow indicates a larger metric value is better.

ADNI dataset						Right WM				
Method	Left WM					EMD (mm) \downarrow	SWD (mm) \downarrow	ASSD (mm) \downarrow	CN \uparrow	SI (%) \downarrow
	EMD (mm) \downarrow	SWD (mm) \downarrow	ASSD (mm) \downarrow	CN \uparrow	SI (%) \downarrow					
DeepCSR [18]	1.368 \pm .721	1.357 \pm 1.178	.390 \pm .162	.934 \pm .016	0	1.350 \pm .350	1.357 \pm .589	.388 \pm .172	.936 \pm .014	0
Vox2Cortex [10]	1.051 \pm .173	.823 \pm .351	.346 \pm .073	.926 \pm .011	.719 \pm .214	1.048 \pm .134	.811 \pm .294	.335 \pm .061	.927 \pm .010	.745 \pm .199
CorticalFlow++ [40]	.912 \pm .435	.525 \pm .265	.271 \pm .071	.936 \pm .009	.058 \pm .032	.821 \pm .169	.473 \pm .286	.268 \pm .073	.933 \pm .009	.067 \pm .032
CortexODE [44]	.803 \pm .136	.436 \pm .403	.234 \pm .064	.938 \pm .010	.013 \pm .011	.782 \pm .081	.384 \pm .259	.231 \pm .052	.939 \pm .009	.004 \pm .005
DD-SWD (ours)	.802 \pm .127	.423 \pm .379	.282 \pm .057	.939 \pm .010	\approx 0	.791 \pm .076	.370 \pm .232	.275 \pm .041	.935 \pm .009	\approx 0

OASIS dataset						Right WM				
Method	Left WM					EMD (mm) \downarrow	SWD (mm) \downarrow	ASSD (mm) \downarrow	CN \uparrow	SI (%) \downarrow
	EMD (mm) \downarrow	SWD (mm) \downarrow	ASSD (mm) \downarrow	CN \uparrow	SI (%) \downarrow					
DeepCSR	.887 \pm .787	1.020 \pm .392	.312 \pm .124	.941 \pm .010	0	.900 \pm .740	1.072 \pm .419	.344 \pm .158	.941 \pm .011	0
Vox2Cortex	.594 \pm .236	.876 \pm .053	.302 \pm .037	.928 \pm .008	.994 \pm .193	.574 \pm .256	.872 \pm .062	.303 \pm .042	.929 \pm .009	1.022 \pm .186
CorticalFlow++	.511 \pm .222	.841 \pm .059	.225 \pm .038	.937 \pm .007	.054 \pm .060	.473 \pm .224	.840 \pm .071	.227 \pm .046	.935 \pm .008	.076 \pm .068
CortexODE	.425 \pm .193	.785 \pm .047	.183 \pm .036	.943 \pm .007	.032 \pm .025	.434 \pm .256	.787 \pm .065	.182 \pm .052	.943 \pm .008	.022 \pm .020
DD-SWD (ours)	.420 \pm .203	.783 \pm .049	.200 \pm .039	.940 \pm .008	\approx 0	.434 \pm .248	.774 \pm .063	.198 \pm .044	.939 \pm .009	\approx 0

Table 2: **White matter surface reconstruction consistency comparison** in terms of EMD, SWD, ASSD on TRT dataset.

Method	EMD	SWD	ASSD
Vox2Cortex	.886 \pm .130	.485 \pm .176	.263 \pm .112
CortexODE	.799 \pm .038	.444 \pm .201	.241 \pm .040
FreeSurfer	.859 \pm .213	.358 \pm .275	.286 \pm .156
DD-SWD	.796 \pm .041	.437 \pm .194	.237 \pm .040

in both EMD and ASSD, and only Freesurfer [25] result has the better performance in SWD score than us.

5.2.2 Qualitative Results

We visualize the reconstructed WM surfaces in ADNI and OASIS datasets. Fig. 3 illustrates the cortical surface meshes with color maps reflecting the point-to-surface errors. We highlight the artifacts of the surface in yellow boxes. Our proposed approach has a reasonably high-quality mesh compared to other methods with fewer artifacts. Specifically, the surfaces reconstructed from CorticalFlow++ [63] and CortexODE [44] often have non-uniform surface effects on the highly curved regions. On the other hand, Vox2Cortex [10] and DeepCSR [18] normally have self-intersections and redundant artifacts.

5.3 Ablation Study

Setups. We evaluate the individual optimization design choices and report the WM surface reconstruction on ADNI dataset. For fair comparisons, we conduct ablation studies on the

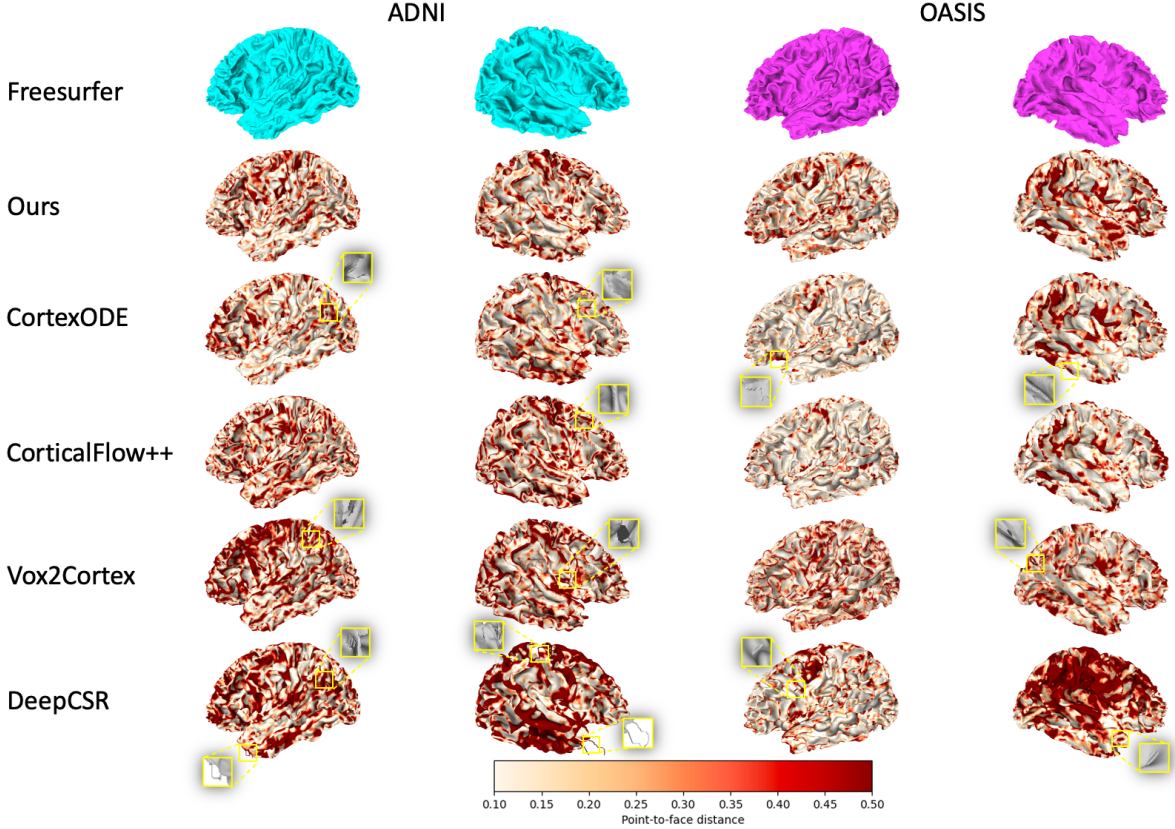


Figure 3: **Qualitative results of white matter surface reconstruction.** The color represents the point-to-face distance, i.e., the darker color is, the further the predicted mesh to the pseudo-ground truth. Artifacts are highlighted by the yellow box. More visualization is given in Appendix E.

same initial surface and the same number of supports, i.e. the number of faces on mesh. We train all of them for 300 epochs and get the best checkpoints on the validation set. The result is reported in Tab. 3 on the holdout test set.

Comparisons. To begin with, we conduct experiments where we independently identically sample points on the surface and used SWD loss to optimize two sets of points. The results showed that this approach did not perform as well as optimizing SWD on oriented varifold representation. This indicates that the varifold method provides better mesh approximation compared to using random points on the surface. In the second part of our ablations, we use CD to optimize two oriented varifolds. Our results show that SWD loss outperforms CD on varifold, which further supports our theorem 1. Finally, we employ the Sinkhorn divergence, implemented by [64], as the loss function to optimize two oriented varifolds. It is worth noting that Sinkhorn divergence is the approximation of Wasserstein distance, but cannot lead to a valid metric between probability measures since the resulting discrepancy does not satisfy the triangle inequality. Experiments on both left and right WM show that our SWD loss outperforms Sinkhorn in both metrics.

Table 3: **Ablation Study** in terms of EMD and SWD metric. *P.S.* and *O.V.* are short for *point sampling* and *oriented varifold* representation, respectively. Best values are highlighted.

	Left WM		Right WM	
	EMD	SWD	EMD	SWD
SWD on P.S.	1.135 \pm .112	.445 \pm .212	1.146 \pm .046	.423 \pm .218
CD on O.V.	.874 \pm .121	.499 \pm .343	.848 \pm .077	.529 \pm .209
Sinkhorn on O.V.	1.023 \pm .109	.578 \pm .307	1.002 \pm .071	.568 \pm .178
SWD on O.V.	.802 \pm .127	.423 \pm .379	.791 \pm .076	.370 \pm .232

6 Conclusion

In this paper, we introduce DD-SWD, a learning-based diffeomorphic deformation network that employs sliced Wasserstein distance (SWD) as the objective function to deform an initial mesh to an intricate mesh based on volumetric input. Different from previous approaches that use point-clouds for approximating mesh, we represent a mesh as a probability measure that generalizes the common set-based methods. By lying on probability measure space, we can further exploit statistical shape analysis theory to approximate mesh as an oriented varifold. Our theorem shows that using SWD to optimize probability measures can have a fast statistical rate for approximating the surfaces of the meshes. Finally, we extensively verify our proposed approach in the challenging brain cortical surface reconstruction problem. Our experiment results demonstrate that our method surpasses existing state-of-the-art competing works in terms of geometric accuracy, self-intersection ratio, and consistency. While our approach is developed within the context of cortical surface reconstruction, it can be adapted to a wide range of 3D deformation frameworks. In the future, we will consider applying more advanced variants of SWD to 3D deformation.

References

- [1] P. Achlioptas, O. Diamanti, I. Mitliagkas, and L. Guibas. Learning representations and generative models for 3d point clouds. In *International conference on machine learning*, pages 40–49. PMLR, 2018.
- [2] F. J. Almgren. *Plateau’s problem: an invitation to varifold geometry*, volume 13. American Mathematical Soc., 1966.
- [3] M. Arjovsky, S. Chintala, and L. Bottou. Wasserstein generative adversarial networks. In *International Conference on Machine Learning*, pages 214–223, 2017.
- [4] V. Arsigny. *Processing data in lie groups: An algebraic approach. Application to non-linear registration and diffusion tensor MRI*. PhD thesis, Citeseer, 2004.
- [5] J. Ashburner. A fast diffeomorphic image registration algorithm. *Neuroimage*, 38(1):95–113, 2007.
- [6] B. B. Avants, C. L. Epstein, M. Grossman, and J. C. Gee. Symmetric diffeomorphic image registration with cross-correlation: evaluating automated labeling of elderly and neurodegenerative brain. *Medical image analysis*, 12(1):26–41, 2008.
- [7] G. Balakrishnan, A. Zhao, M. R. Sabuncu, J. Guttag, and A. V. Dalca. Voxelmorph: a learning framework for deformable medical image registration. *IEEE transactions on medical imaging*, 38(8):1788–1800, 2019.
- [8] H. G. Barrow, J. M. Tenenbaum, R. C. Bolles, and H. C. Wolf. Parametric correspondence and chamfer matching: Two new techniques for image matching. Technical report, SRI INTERNATIONAL MENLO PARK CA ARTIFICIAL INTELLIGENCE CENTER, 1977.
- [9] E. Bernton, P. E. Jacob, M. Gerber, and C. P. Robert. On parameter estimation with the Wasserstein distance. *Information and Inference: A Journal of the IMA*, 8(4):657–676, 2019.
- [10] F. Bongratz, A.-M. Rickmann, S. Pölsterl, and C. Wachinger. Vox2cortex: fast explicit reconstruction of cortical surfaces from 3d mri scans with geometric deep neural networks. In *Proceedings of the IEEE/CVF Conference on Computer Vision and Pattern Recognition*, pages 20773–20783, 2022.
- [11] N. Bonneel, J. Rabin, G. Peyré, and H. Pfister. Sliced and radon Wasserstein barycenters of measures. *Journal of Mathematical Imaging and Vision*, 51:22–45, 2015.
- [12] N. Charon. *Analysis of geometric and functional shapes with extensions of currents: applications to registration and atlas estimation*. PhD thesis, École normale supérieure de Cachan-ENS Cachan, 2013.
- [13] N. Charon and A. Trounev. The varifold representation of nonoriented shapes for diffeomorphic registration. *SIAM journal on Imaging Sciences*, 6(4):2547–2580, 2013.

- [14] R. T. Chen, Y. Rubanova, J. Bettencourt, and D. K. Duvenaud. Neural ordinary differential equations. *Advances in neural information processing systems*, 31, 2018.
- [15] Z. Chen and H. Zhang. Learning implicit fields for generative shape modeling. In *Proceedings of the IEEE/CVF Conference on Computer Vision and Pattern Recognition*, pages 5939–5948, 2019.
- [16] C. B. Choy, D. Xu, J. Gwak, K. Chen, and S. Savarese. 3d-r2n2: A unified approach for single and multi-view 3d object reconstruction. In *Computer Vision–ECCV 2016: 14th European Conference, Amsterdam, The Netherlands, October 11–14, 2016, Proceedings, Part VIII 14*, pages 628–644. Springer, 2016.
- [17] E. A. Coddington and N. Levinson. *Theory of ordinary differential equations*. Pure & Applied Mathematics S. McGraw-Hill Education, London, England, Mar. 1984.
- [18] R. S. Cruz, L. Lebrat, P. Bourgeat, C. Fookes, J. Fripp, and O. Salvado. Deepcsr: A 3d deep learning approach for cortical surface reconstruction. In *Proceedings of the IEEE/CVF Winter Conference on Applications of Computer Vision*, pages 806–815, 2021.
- [19] M. Cuturi. Sinkhorn distances: Lightspeed computation of optimal transport. In *Advances in Neural Information Processing Systems*, pages 2292–2300, 2013.
- [20] A. V. Dalca, G. Balakrishnan, J. Guttag, and M. R. Sabuncu. Unsupervised learning for fast probabilistic diffeomorphic registration. In *International Conference on Medical Image Computing and Computer-Assisted Intervention*, pages 729–738. Springer, 2018.
- [21] A. V. Dalca, G. Balakrishnan, J. Guttag, and M. R. Sabuncu. Unsupervised learning of probabilistic diffeomorphic registration for images and surfaces. *Medical image analysis*, 57:226–236, 2019.
- [22] H. Deng, T. Birdal, and S. Ilic. Ppf-foldnet: Unsupervised learning of rotation invariant 3d local descriptors. In *Proceedings of the European conference on computer vision (ECCV)*, pages 602–618, 2018.
- [23] C. Duan, S. Chen, and J. Kovacevic. 3d point cloud denoising via deep neural network based local surface estimation. In *ICASSP 2019-2019 IEEE International Conference on Acoustics, Speech and Signal Processing (ICASSP)*, pages 8553–8557. IEEE, 2019.
- [24] J. Feydy, T. Séjourné, F.-X. Vialard, S.-i. Amari, A. Trounev, and G. Peyré. Interpolating between optimal transport and MMD using Sinkhorn divergences. In *The 22nd International Conference on Artificial Intelligence and Statistics*, pages 2681–2690, 2019.
- [25] B. Fischl. Freesurfer. *Neuroimage*, 62(2):774–781, 2012.
- [26] J. Glaunès, A. Qiu, M. I. Miller, and L. Younes. Large deformation diffeomorphic metric curve mapping. *International journal of computer vision*, 80:317–336, 2008.
- [27] J. Glaunès, A. Trounev, and L. Younes. Diffeomorphic matching of distributions: A new approach for unlabelled point-sets and sub-manifolds matching. In *Proceedings of the 2004 IEEE Computer Society Conference on Computer Vision and Pattern Recognition, 2004. CVPR 2004.*, volume 2, pages II–II. IEEE, 2004.

- [28] Z. Goldfeld, K. Kato, G. Rioux, and R. Sadhu. Statistical inference with regularized optimal transport. *arXiv preprint arXiv:2205.04283*, 2022.
- [29] T. Groueix, M. Fisher, V. G. Kim, B. C. Russell, and M. Aubry. A papier-mâché approach to learning 3d surface generation. In *Proceedings of the IEEE conference on computer vision and pattern recognition*, pages 216–224, 2018.
- [30] K. Gupta. *Neural mesh flow: 3d manifold mesh generation via diffeomorphic flows*. University of California, San Diego, 2020.
- [31] K. Han, S. Sun, X. Yan, C. You, H. Tang, J. Naushad, H. Ma, D. Kong, and X. Xie. Diffeomorphic image registration with neural velocity field. In *Proceedings of the IEEE/CVF Winter Conference on Applications of Computer Vision*, pages 1869–1879, 2023.
- [32] C. Häne, S. Tulsiani, and J. Malik. Hierarchical surface prediction for 3d object reconstruction. In *2017 International Conference on 3D Vision (3DV)*, pages 412–420. IEEE, 2017.
- [33] H.-W. Hsieh and N. Charon. Diffeomorphic registration of discrete geometric distributions. In *Mathematics Of Shapes And Applications*, pages 45–74. World Scientific, 2020.
- [34] C. R. Jack Jr, M. A. Bernstein, N. C. Fox, P. Thompson, G. Alexander, D. Harvey, B. Borowski, P. J. Britson, J. L. Whitwell, C. Ward, et al. The alzheimer’s disease neuroimaging initiative (adni): Mri methods. *Journal of Magnetic Resonance Imaging: An Official Journal of the International Society for Magnetic Resonance in Medicine*, 27(4):685–691, 2008.
- [35] C. Jiang, A. Sud, A. Makadia, J. Huang, M. Nießner, T. Funkhouser, et al. Local implicit grid representations for 3d scenes. In *Proceedings of the IEEE/CVF Conference on Computer Vision and Pattern Recognition*, pages 6001–6010, 2020.
- [36] I. Kaltenmark, B. Charlier, and N. Charon. A general framework for curve and surface comparison and registration with oriented varifolds. In *Proceedings of the IEEE Conference on Computer Vision and Pattern Recognition*, pages 3346–3355, 2017.
- [37] D. P. Kingma and J. Ba. Adam: A method for stochastic optimization. *arXiv preprint arXiv:1412.6980*, 2014.
- [38] A. Korotin, L. Li, A. Genevay, J. M. Solomon, A. Filippov, and E. Burnaev. Do neural optimal transport solvers work? a continuous Wasserstein-2 benchmark. *Advances in Neural Information Processing Systems*, 34:14593–14605, 2021.
- [39] J. Krebs, H. Delingette, B. Mailhé, N. Ayache, and T. Mansi. Learning a probabilistic model for diffeomorphic registration. *IEEE transactions on medical imaging*, 38(9):2165–2176, 2019.
- [40] L. Lebrat, R. Santa Cruz, F. de Gournay, D. Fu, P. Bourgeat, J. Fripp, C. Fookes, and O. Salvado. Corticalflow: a diffeomorphic mesh transformer network for cortical surface reconstruction. *Advances in Neural Information Processing Systems*, 34:29491–29505, 2021.

- [41] L. Lebrat, R. Santa Cruz, F. de Gournay, D. Fu, P. Bourgeat, J. Fripp, C. Fookes, and O. Salvado. Corticalflow: A diffeomorphic mesh deformation module for cortical surface reconstruction. *arXiv preprint arXiv:2206.02374*, 2022.
- [42] W. E. Lorensen and H. E. Cline. Marching cubes: A high resolution 3d surface construction algorithm. *ACM siggraph computer graphics*, 21(4):163–169, 1987.
- [43] J. Ma, M. I. Miller, and L. Younes. A Bayesian generative model for surface template estimation. *Journal of Biomedical Imaging*, 2010:1–14, 2010.
- [44] Q. Ma, L. Li, E. C. Robinson, B. Kainz, D. Rueckert, and A. Alansary. Cortexode: Learning cortical surface reconstruction by Neural ODEs. *IEEE Transactions on Medical Imaging*, 2022.
- [45] Q. Ma, E. C. Robinson, B. Kainz, D. Rueckert, and A. Alansary. Pialnn: a fast deep learning framework for cortical pial surface reconstruction. In *Machine Learning in Clinical Neuroimaging: 4th International Workshop, MLCN 2021, Held in Conjunction with MICCAI 2021, Strasbourg, France, September 27, 2021, Proceedings 4*, pages 73–81. Springer, 2021.
- [46] J. Maclaren, Z. Han, S. B. Vos, N. Fischbein, and R. Bammer. Reliability of brain volume measurements: a test-retest dataset. *Scientific data*, 1(1):1–9, 2014.
- [47] D. S. Marcus, T. H. Wang, J. Parker, J. G. Csernansky, J. C. Morris, and R. L. Buckner. Open access series of imaging studies (oasis): cross-sectional mri data in young, middle aged, nondemented, and demented older adults. *Journal of cognitive neuroscience*, 19(9):1498–1507, 2007.
- [48] G. Mena and J. Weed. Statistical bounds for entropic optimal transport: sample complexity and the central limit theorem. In *Advances in Neural Information Processing Systems*, 2019.
- [49] L. Mescheder, M. Oechsle, M. Niemeyer, S. Nowozin, and A. Geiger. Occupancy networks: Learning 3d reconstruction in function space. In *Proceedings of the IEEE/CVF conference on computer vision and pattern recognition*, pages 4460–4470, 2019.
- [50] K. Nguyen and N. Ho. Control variate sliced Wasserstein estimators. *arXiv preprint arXiv:2305.00402*, 2023.
- [51] K. Nguyen and N. Ho. Energy-based sliced Wasserstein distance. *arXiv preprint arXiv:2304.13586*, 2023.
- [52] K. Nguyen, N. Ho, T. Pham, and H. Bui. Distributional sliced-Wasserstein and applications to generative modeling. In *International Conference on Learning Representations*, 2021.
- [53] K. Nguyen, D. Nguyen, and N. Ho. Self-attention amortized distributional projection optimization for sliced Wasserstein point-cloud reconstruction. *Proceedings of the 40th International Conference on Machine Learning*, 2023.

- [54] T. Nguyen, Q.-H. Pham, T. Le, T. Pham, N. Ho, and B.-S. Hua. Point-set distances for learning representations of 3d point clouds. In *Proceedings of the IEEE/CVF International Conference on Computer Vision (ICCV)*, 2021.
- [55] M. Niemeyer, L. Mescheder, M. Oechsle, and A. Geiger. Differentiable volumetric rendering: Learning implicit 3d representations without 3d supervision. In *Proceedings of the IEEE/CVF Conference on Computer Vision and Pattern Recognition*, pages 3504–3515, 2020.
- [56] J. Pan, X. Han, W. Chen, J. Tang, and K. Jia. Deep mesh reconstruction from single rgb images via topology modification networks. In *Proceedings of the IEEE/CVF International Conference on Computer Vision*, pages 9964–9973, 2019.
- [57] J. J. Park, P. Florence, J. Straub, R. Newcombe, and S. Lovegrove. Deepsdf: Learning continuous signed distance functions for shape representation. In *Proceedings of the IEEE/CVF conference on computer vision and pattern recognition*, pages 165–174, 2019.
- [58] S. Peng, M. Niemeyer, L. Mescheder, M. Pollefeys, and A. Geiger. Convolutional occupancy networks. In *Computer Vision–ECCV 2020: 16th European Conference, Glasgow, UK, August 23–28, 2020, Proceedings, Part III 16*, pages 523–540. Springer, 2020.
- [59] G. Peyré and M. Cuturi. Computational optimal transport: With applications to data science. *Foundations and Trends® in Machine Learning*, 11(5-6):355–607, 2019.
- [60] N. Ravi, J. Reizenstein, D. Novotny, T. Gordon, W.-Y. Lo, J. Johnson, and G. Gkioxari. Accelerating 3d deep learning with pytorch3d. *arXiv:2007.08501*, 2020.
- [61] I. Rekik, G. Li, W. Lin, and D. Shen. Multidirectional and topography-based dynamic-scale varifold representations with application to matching developing cortical surfaces. *NeuroImage*, 135:152–162, 2016.
- [62] D. Ruelle and D. Sullivan. Currents, flows and diffeomorphisms. *Topology*, 14(4):319–327, 1975.
- [63] R. Santa Cruz, L. Lebrat, D. Fu, P. Bourgeat, J. Fripp, C. Fookes, and O. Salvado. Corticalflow++: Boosting cortical surface reconstruction accuracy, regularity, and interoperability. In *Medical Image Computing and Computer Assisted Intervention–MICCAI 2022: 25th International Conference, Singapore, September 18–22, 2022, Proceedings, Part V*, pages 496–505. Springer, 2022.
- [64] T. Séjourné, J. Feydy, F.-X. Vialard, A. Trounev, and G. Peyré. Sinkhorn divergences for unbalanced optimal transport. *arXiv preprint arXiv:1910.12958*, 2019.
- [65] E. J. Smith, S. Fujimoto, A. Romero, and D. Meger. Geometrics: Exploiting geometric structure for graph-encoded objects. *arXiv preprint arXiv:1901.11461*, 2019.
- [66] S. Sun, K. Han, D. Kong, H. Tang, X. Yan, and X. Xie. Topology-preserving shape reconstruction and registration via neural diffeomorphic flow. In *Proceedings of the IEEE/CVF Conference on Computer Vision and Pattern Recognition*, pages 20845–20855, 2022.

- [67] M. Tatarchenko, A. Dosovitskiy, and T. Brox. Octree generating networks: Efficient convolutional architectures for high-resolution 3d outputs. In *Proceedings of the IEEE international conference on computer vision*, pages 2088–2096, 2017.
- [68] M. Vaillant and J. Glaunes. Surface matching via currents. In *Information Processing in Medical Imaging: 19th International Conference, IPMI 2005, Glenwood Springs, CO, USA, July 10-15, 2005. Proceedings 19*, pages 381–392. Springer, 2005.
- [69] C. Villani. *Topics in optimal transportation*. Number 58. American Mathematical Soc., 2003.
- [70] C. Villani. *Optimal transport: old and new*, volume 338. Springer, 2009.
- [71] M. J. Wainwright. *High-dimensional statistics: A non-asymptotic viewpoint*. Cambridge University Press, 2019.
- [72] N. Wang, Y. Zhang, Z. Li, Y. Fu, W. Liu, and Y.-G. Jiang. Pixel2mesh: Generating 3d mesh models from single rgb images. In *Proceedings of the European conference on computer vision (ECCV)*, pages 52–67, 2018.
- [73] P.-S. Wang, C.-Y. Sun, Y. Liu, and X. Tong. Adaptive o-cnn: A patch-based deep representation of 3d shapes. *ACM Transactions on Graphics (TOG)*, 37(6):1–11, 2018.
- [74] W. Wang, D. Ceylan, R. Mech, and U. Neumann. 3dn: 3d deformation network. In *Proceedings of the IEEE/CVF Conference on Computer Vision and Pattern Recognition*, pages 1038–1046, 2019.
- [75] U. Wickramasinghe, E. Remelli, G. Knott, and P. Fua. Voxel2mesh: 3d mesh model generation from volumetric data. In *Medical Image Computing and Computer Assisted Intervention—MICCAI 2020: 23rd International Conference, Lima, Peru, October 4–8, 2020, Proceedings, Part IV 23*, pages 299–308. Springer, 2020.
- [76] Q. Xu, W. Wang, D. Ceylan, R. Mech, and U. Neumann. Disn: Deep implicit surface network for high-quality single-view 3d reconstruction. *Advances in neural information processing systems*, 32, 2019.
- [77] L. Yariv, Y. Kasten, D. Moran, M. Galun, M. Atzmon, B. Ronen, and Y. Lipman. Multiview neural surface reconstruction by disentangling geometry and appearance. *Advances in Neural Information Processing Systems*, 33:2492–2502, 2020.
- [78] Q. Zhou. Pymesh—geometry processing library for python. *Software available for download at <https://github.com/PyMesh/PyMesh>*, 2019.

Supplement to “Diffeomorphic Deformation via Sliced Wasserstein Distance Optimization for Cortical Surface Reconstruction”

In this supplementary, we first provide additional materials in Appendix A including the detailed setup and more insight about our toy example mentioned in Fig. 1. Secondly, we demonstrate complete proof for the Theorem 1 in Appendix B. Next, we delve into the implementation details in Appendix C and provide detailed information about the datasets in Appendix D. We also present additional visualization of our experiment results in Appendix E. Finally, we discuss the potential impact, limitations, and future work that we plan to undertake as a follow-up to this research in Appendix F.

A Toy Examples

Setups. In this toy example, we aim to deform the template circle to the target polygon in an optimization-based. We uniformly sample the template circle and the target polygon into 2D points. The number of sampled points on both the template circle and target polygon are 678 points. To optimize the position of predicted points and target points, we employ Chamfer loss implemented by [60], and the sliced Wasserstein distance with $p = 2$ approximated by Monte Carlo estimation with 100 projections. We optimize the two sets of points with stochastic gradient descent (SGD) optimizer with a learning rate of 1.0 and momentum of 0.9 for 1000 iterations.

Discussion. As shown in Fig. 4, we can see that the set of points optimized by Chamfer distance often gets trapped in some specific region, e.g. the acute region of the polygon in this example. This confinement occurs due to the nature of Chamfer distance, which primarily focuses on optimizing nearest neighbors, inhibiting the points from escaping the local region during the optimization process. To alleviate this issue, practitioners often introduce multiple losses as regularizers to aid Chamfer distance in escaping local minima. However, determining the appropriate weights for each auxiliary loss is a challenging task, as they tend to vary across different tasks, thus making the optimization process harder. SWD loss, on the other hand, can find the optimal transport plan for the whole set of points, thus resulting in a better solution when compared to Chamfer distance.

B Proof of Theorem 1

Using the triangle inequality of the \mathbb{L}_1 norm, we obtain:

$$\begin{aligned} \mathbb{E} \left[\left| \widehat{\text{SW}}_p^p(\hat{\mu}_m^{\mathcal{M}_1}, \hat{\mu}_m^{\mathcal{M}_2}; L) - \text{SW}_p^p(\mu^{\mathcal{M}_1}, \mu^{\mathcal{M}_2}) \right| \right] &\leq \mathbb{E} \left[\left| \widehat{\text{SW}}_p^p(\hat{\mu}_m^{\mathcal{M}_1}, \hat{\mu}_m^{\mathcal{M}_2}; L) - \text{SW}_p^p(\hat{\mu}_m^{\mathcal{M}_1}, \hat{\mu}_m^{\mathcal{M}_2}) \right| \right] \\ &\quad + \mathbb{E} \left[\left| \text{SW}_p^p(\hat{\mu}_m^{\mathcal{M}_1}, \hat{\mu}_m^{\mathcal{M}_2}) - \text{SW}_p^p(\mu^{\mathcal{M}_1}, \mu^{\mathcal{M}_2}) \right| \right]. \end{aligned}$$

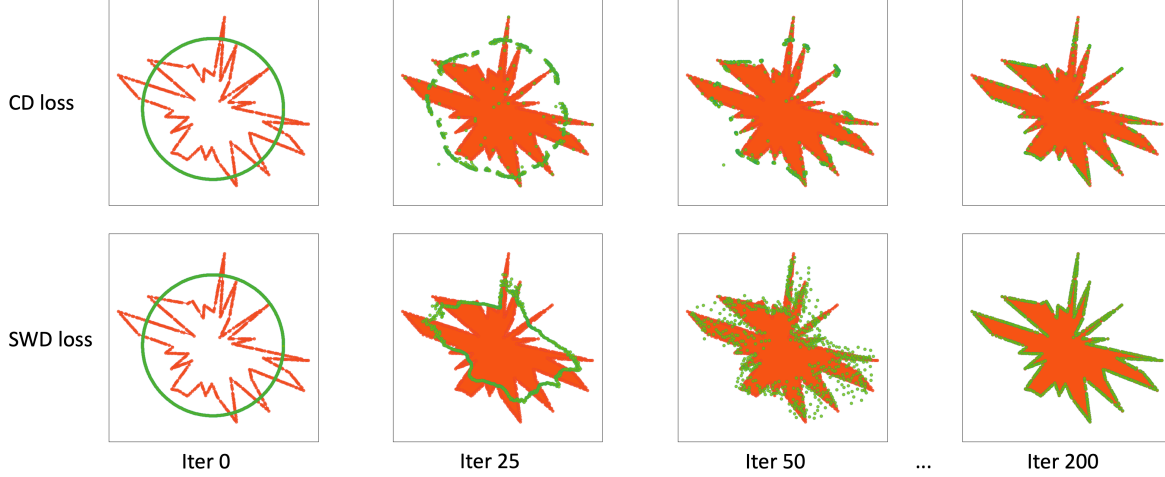


Figure 4: **Visualization of the optimization process of 2D toy example.** The set of green points, i.e. sampled points from the template circle, optimized by CD loss often concentrates around the acute region of the polygon and easily gets trapped at some local regions. Nonetheless, the set of points optimized by SWD loss distributes more uniformly along the edge of the polygon, thus making the optimization process more robust.

Now, we bound the first term $\mathbb{E} \left[\left| \widehat{\text{SW}}_p^p(\hat{\mu}_m^{\mathcal{M}_1}, \hat{\mu}_m^{\mathcal{M}_2}; L) - \text{SW}_p^p(\hat{\mu}_m^{\mathcal{M}_1}, \hat{\mu}_m^{\mathcal{M}_2}) \right| \right]$. By the definitions of the SW and its Monte Carlo estimation, we have:

$$\begin{aligned}
& \mathbb{E} \left[\left| \widehat{\text{SW}}_p^p(\hat{\mu}_m^{\mathcal{M}_1}, \hat{\mu}_m^{\mathcal{M}_2}; L) - \text{SW}_p^p(\hat{\mu}_m^{\mathcal{M}_1}, \hat{\mu}_m^{\mathcal{M}_2}) \right| \right] \\
&= \mathbb{E} \left[\left| \frac{1}{L} \sum_{l=1}^L W_p^p(\theta_l \# \hat{\mu}_m^{\mathcal{M}_1}, \theta_l \# \hat{\mu}_m^{\mathcal{M}_2}) - \mathbb{E}[W_p^p(\theta \# \hat{\mu}_m^{\mathcal{M}_1}, \theta \# \hat{\mu}_m^{\mathcal{M}_2}) | X_{1:m}, Y_{1:m}] \right| \right] \\
&\leq \left(\mathbb{E} \left[\left(\frac{1}{L} \sum_{l=1}^L W_p^p(\theta_l \# \hat{\mu}_m^{\mathcal{M}_1}, \theta_l \# \hat{\mu}_m^{\mathcal{M}_2}) - \mathbb{E}[W_p^p(\theta \# \hat{\mu}_m^{\mathcal{M}_1}, \theta \# \hat{\mu}_m^{\mathcal{M}_2}) | X_{1:m}, Y_{1:m}] \right)^2 \right] \right)^{\frac{1}{2}} \\
&= \left(\mathbb{E} \left[\left(\frac{1}{L} \sum_{l=1}^L (W_p^p(\theta_l \# \hat{\mu}_m^{\mathcal{M}_1}, \theta_l \# \hat{\mu}_m^{\mathcal{M}_2}) - \mathbb{E}[W_p^p(\theta \# \hat{\mu}_m^{\mathcal{M}_1}, \theta \# \hat{\mu}_m^{\mathcal{M}_2}) | X_{1:m}, Y_{1:m}]) \right)^2 \right] \right)^{\frac{1}{2}},
\end{aligned}$$

where the inequality is due to the Holder's inequality. Using the fact that

$$\mathbb{E} \left[\frac{1}{L} \sum_{l=1}^L W_p^p(\theta_l \# \hat{\mu}_m^{\mathcal{M}_1}, \theta_l \# \hat{\mu}_m^{\mathcal{M}_2}) | X_{1:m}, Y_{1:m} \right] = \mathbb{E}[W_p^p(\theta \# \hat{\mu}_m^{\mathcal{M}_1}, \theta \# \hat{\mu}_m^{\mathcal{M}_2}) | X_{1:m}, Y_{1:m}] \text{ since } \theta_1, \dots, \theta_L \stackrel{i.i.d}{\sim} \mathcal{U}(\mathbb{S}^{d-1}), \text{ we have:}$$

$$\begin{aligned}
\mathbb{E} \left[\left| \widehat{\text{SW}}_p^p(\hat{\mu}_m^{\mathcal{M}_1}, \hat{\mu}_m^{\mathcal{M}_2}; L) - \text{SW}_p^p(\hat{\mu}_m^{\mathcal{M}_1}, \hat{\mu}_m^{\mathcal{M}_2}) \right| \right] &\leq \left(\text{Var} \left[\left(\frac{1}{L} \sum_{l=1}^L W_p^p(\theta_l \# \hat{\mu}_m^{\mathcal{M}_1}, \theta_l \# \hat{\mu}_m^{\mathcal{M}_2}) | X_{1:m}, Y_{1:m} \right) \right] \right)^{\frac{1}{2}} \\
&= \frac{1}{\sqrt{L}} \text{Var} [W_p^p(\theta \# \hat{\mu}_m^{\mathcal{M}_1}, \theta \# \hat{\mu}_m^{\mathcal{M}_2}) | X_{1:m}, Y_{1:m}]^{\frac{1}{2}}.
\end{aligned}$$

Now, we bound the second term $\mathbb{E} [|\text{SW}_p^p(\hat{\mu}_m^{\mathcal{M}_1}, \hat{\mu}_m^{\mathcal{M}_2}) - \text{SW}_p^p(\mu^{\mathcal{M}_1}, \mu^{\mathcal{M}_2})|]$. Using the Jensen inequality, we obtain

$$\begin{aligned} \mathbb{E} [|\text{SW}_p^p(\hat{\mu}_m^{\mathcal{M}_1}, \hat{\mu}_m^{\mathcal{M}_2}) - \text{SW}_p^p(\mu^{\mathcal{M}_1}, \mu^{\mathcal{M}_2})|] &= \mathbb{E} [|\mathbb{E}[\text{W}_p^p(\theta_{\#}^{\hat{\mu}_m^{\mathcal{M}_1}}, \theta_{\#}^{\hat{\mu}_m^{\mathcal{M}_2}})] - \mathbb{E}[\text{W}_p^p(\theta_{\#}^{\mu^{\mathcal{M}_1}}, \theta_{\#}^{\mu^{\mathcal{M}_2}})]|] \\ &\leq \mathbb{E} [|\text{W}_p^p(\theta_{\#}^{\hat{\mu}_m^{\mathcal{M}_1}}, \theta_{\#}^{\hat{\mu}_m^{\mathcal{M}_2}}) - \text{W}_p^p(\theta_{\#}^{\mu^{\mathcal{M}_1}}, \theta_{\#}^{\mu^{\mathcal{M}_2}})|] \\ &\leq C_{p,R}^{(1)} \mathbb{E} [|\text{W}_1(\theta_{\#}^{\hat{\mu}_m^{\mathcal{M}_1}}, \theta_{\#}^{\mu^{\mathcal{M}_1}}) + \text{W}_1(\theta_{\#}^{\hat{\mu}_m^{\mathcal{M}_2}}, \theta_{\#}^{\mu^{\mathcal{M}_2}})|] \\ &= C_{p,R}^{(1)} (\mathbb{E}[\text{W}_1(\theta_{\#}^{\hat{\mu}_m^{\mathcal{M}_1}}, \theta_{\#}^{\mu^{\mathcal{M}_1}})] + \mathbb{E}[\text{W}_1(\theta_{\#}^{\hat{\mu}_m^{\mathcal{M}_2}}, \theta_{\#}^{\mu^{\mathcal{M}_2}})]), \end{aligned}$$

where the second inequality is due to Lemma 4 in [28]. We now show that:

$$\mathbb{E}[\text{W}_1(\theta_{\#}^{\hat{\mu}_m^{\mathcal{M}_1}}, \theta_{\#}^{\mu^{\mathcal{M}_1}})] \leq C_R^{(2)} \sqrt{\frac{(d+1) \log m}{m}}.$$

Following [52, 51], we have:

$$\begin{aligned} \mathbb{E}[\text{W}_1(\theta_{\#}^{\hat{\mu}_m^{\mathcal{M}_1}}, \theta_{\#}^{\mu^{\mathcal{M}_1}})] &\leq \mathbb{E} \left[\max_{\theta \in \mathbb{S}^{d-1}} \text{W}_1(\theta_{\#}^{\hat{\mu}_m^{\mathcal{M}_1}}, \theta_{\#}^{\mu^{\mathcal{M}_1}}) | X_{1:m}, Y_{1:m} \right] \\ &= \mathbb{E} \left[\max_{\theta \in \mathbb{R}^d, \|\theta\|_2 \leq 1} \text{W}_1(\theta_{\#}^{\hat{\mu}_m^{\mathcal{M}_1}}, \theta_{\#}^{\mu^{\mathcal{M}_1}}) | X_{1:m}, Y_{1:m} \right] \\ &= \mathbb{E} \left[\max_{\theta \in \mathbb{R}^d, \|\theta\|_2 \leq 1} \int_0^1 |F_{m,\theta}^{-1}(z) - F_{\theta}^{-1}(z)| dz | X_{1:m}, Y_{1:m} \right], \end{aligned}$$

where $F_{m,\theta}^{-1}(z)$ is the inverse CDF of $\hat{\mu}_m^{\mathcal{M}_1}$, $F_{\theta}^{-1}(z)$ is the inverse CDF of $\mu^{\mathcal{M}_1}$. Using the assumption that the diameter of $\mu^{\mathcal{M}_1}$ is at most R , we have:

$$\begin{aligned} &\mathbb{E} \left[\max_{\theta \in \mathbb{R}^d, \|\theta\|_2 \leq 1} \int_0^1 |F_{m,\theta}^{-1}(z) - F_{\theta}^{-1}(z)| dz | X_{1:m}, Y_{1:m} \right] \\ &= \mathbb{E} \left[\max_{\theta \in \mathbb{R}^d, \|\theta\|_2 \leq 1} \int_{-\infty}^{\infty} |F_{m,\theta}(y) - F_{\theta}(y)| dy | X_{1:m}, Y_{1:m} \right] \\ &\leq R \mathbb{E} \left[\sup_{y \in \mathbb{R}, \theta \in \mathbb{R}^d, \|\theta\|_2 \leq 1} |F_{m,\theta}(y) - F_{\theta}(y)| \right] \\ &= R \mathbb{E} \left[\sup_{C \in \mathcal{B}} |\hat{\mu}_m^{\mathcal{M}_1}(C) - \mu^{\mathcal{M}_1}(C)| \right], \end{aligned}$$

where $\mathcal{B} = \{x \in \mathbb{R}^d | \theta^\top x \leq y\}$ is set of half spaces for θ and y . Since the Vapnik-Chervonenkis (VC) dimension of \mathcal{B} is upper bounded by $d+1$ [71], applying the VC inequality results:

$$\mathbb{E} \left[\sup_{C \in \mathcal{B}} |\hat{\mu}_m^{\mathcal{M}_1}(C) - \mu^{\mathcal{M}_1}(C)| \right] \leq C \sqrt{\frac{(d+1) \log m}{m}},$$

for a constant $C > 0$. Absorbing constants, we obtain the final result. Therefore, we conclude the proof.

Algorithm 1 Training cortical surface reconstruction with SWD distance

Input: MRI volume \mathbf{I} , initial mesh $\mathcal{M}_0 = (\mathcal{V}_0, \mathcal{F})$, learning rate η , max iter T , number projections L .

Initialization: Deformation network $\mathbb{F}_\phi(\mathbf{I}, \mathcal{M}_0)$.

while ϕ not converge or reach T **do**

$\nabla_\phi \leftarrow 0$

\triangleright Zero gradient.

$\hat{\mathcal{V}} \leftarrow \text{ODESolver}(\mathbb{F}_\phi, \mathcal{V}_0)$

\triangleright Deform source vertices \mathcal{V}_0 to $\hat{\mathcal{V}}$.

$\hat{\mathcal{M}} \leftarrow (\hat{\mathcal{V}}, \mathcal{F})$

\triangleright Get predicted mesh.

$\tilde{\mu}^{\hat{\mathcal{M}}} \leftarrow \text{ToMeasure}(\hat{\mathcal{M}}); \tilde{\mu}^{\mathcal{M}^*} \leftarrow \text{ToMeasure}(\mathcal{M}^*)$

\triangleright Transform to discrete measures.

$\nabla_\phi \leftarrow \nabla_\phi + \frac{1}{L} \sum_{l=1}^L \nabla_\phi W_p^p(\theta_{l\#} \tilde{\mu}^{\hat{\mathcal{M}}}, \theta_{l\#} \tilde{\mu}^{\mathcal{M}^*})$

\triangleright Update gradient.

$\phi \leftarrow \phi - \eta \cdot \nabla_\phi$

\triangleright Update parameters.

end while

Return: $\phi_{\mathcal{M} \rightarrow \mathcal{M}^*}$

C Implementation Details

Network architecture. First of all, for the white matter segmentation model, we train a vanilla 3D U-Net model with sequential 3D convolutional layers with kernel size $3 \times 3 \times 3$. Secondly, for the deformation network, for each $v_0 \in \mathbb{R}^3$, we linearly transform it to a 128-dimensional feature vector. For each v_0 , we find a corresponding cube size $5 \times 5 \times 5$ on \mathbf{I} . This process can be repeated across multiple scales of \mathbf{I} , resulting in the extraction of multiple cubes. Then, we apply a 3D convolution layer followed by a linear layer to transform the spatial cubes to a 128-dimensional feature vector, i.e. same as the feature of v_0 . Once having the v_0 's features and its corresponding spatial features, we concatenate them as a new feature before passing through an MLP, namely \mathbb{F}_ϕ , to learn the deformation. As discussed, we represent the predicted mesh $\hat{\mathcal{M}}$ and the target mesh \mathcal{M}^* as probability measures $\mu^{\hat{\mathcal{M}}}$ and $\mu^{\mathcal{M}^*}$, respectively. In practice, we can substitute discrete probability measures, e.g. oriented varifold, as $\tilde{\mu}^{\hat{\mathcal{M}}}$ and $\tilde{\mu}^{\mathcal{M}^*}$, respectively. The loss function is computed as follows:

$$\mathcal{L}(\hat{\mathcal{M}}, \mathcal{M}^*) = \widehat{SW}_p^p(\tilde{\mu}^{\hat{\mathcal{M}}}, \tilde{\mu}^{\mathcal{M}^*}) = \frac{1}{L} \sum_{l=1}^L W_p^p(\theta_{l\#} \tilde{\mu}^{\hat{\mathcal{M}}}, \theta_{l\#} \tilde{\mu}^{\mathcal{M}^*}),$$

where $W_p^p(\theta_{l\#} \tilde{\mu}^{\hat{\mathcal{M}}}, \theta_{l\#} \tilde{\mu}^{\mathcal{M}^*})$ is the Wasserstein- p [69] distance between $\tilde{\mu}^{\hat{\mathcal{M}}}$ and $\tilde{\mu}^{\mathcal{M}^*}$. We fix $L = 100, p = 2$ for all of our experiments. In terms of oriented varifold, for each support, we concatenate the barycenter of vertices of the face and the unit normal vector as a single vector in \mathbb{R}^6 . The training procedure is described in Algo. 1.

Training details. We optimize both segmentation and deformation networks with Adam optimizer [37] with a fixed learning rate 10^{-4} . We train the segmentation and the deformation networks for 100 and 300 epochs, respectively, and get the best checkpoint on the validation set. All experiments are implemented using Pytorch and executed on a system equipped with an NVIDIA RTX A6000 GPU and an Intel i7-7700K CPU.

D Dataset Information

As discussed in Sec. 5.1, we employ three publicly available datasets: the Alzheimer’s Disease Neuroimaging Initiative (ADNI) dataset [34], the Open Access Series of Imaging Studies (OASIS) dataset [47], and the test-retest (TRT) dataset [46]. A subset of the ADNI dataset [34] is employed, consisting of 419 T1-weighted (T1w) brain MRI from subjects aged from 55 to 90 years old. The dataset is stratified into 299 scans for training ($\approx 70\%$), 40 scans for validation ($\approx 10\%$), and 80 scans for testing ($\approx 20\%$). Regarding the OASIS dataset [47], all 416 T1-weighted (T1w) brain MRI images are included. We stratify the dataset into 292 scans for training ($\approx 70\%$), 44 scans for validation ($\approx 10\%$), and 80 scans for testing ($\approx 20\%$). As for the TRT dataset [46], it consists of 120 scans obtained from three distinct subjects, with each subject undergoing two scans within a span of 20 days.

E Visualizations

We provide more visualization of our work as in Fig. 5 and Fig. 6. We randomly select the prediction meshes from the test set and compute the point-to-surface distance. The color is encoded as how far the point is to the surface. The figures say that the darker color is, the further the predicted mesh to the pseudo-ground truth.

F Potential Impacts and Limitation

Potential impacts. Our work experiments on the human brain MRI dataset. Our proposed model holds the potential to assist neuroradiologists in effectively visualizing brain surfaces. However, it is crucial to emphasize that our predictions should not be utilized for making clinical decisions. This is because our model has solely undergone testing using the data discussed within this research, and we cannot ensure its performance on unseen data in clinical practices.

Limitations. One limitation we encountered in our study relates to the running time. Specifically, while the Chamfer distance (CD) exhibits a quadratic time complexity in relation to the number of supports, and the sliced Wasserstein distance (SWD) demonstrates near-linear time complexity, i.e. $\mathcal{O}(m \log m)$, our practical observations indicate that they execute in nearly the same duration. This occurrence can be attributed to our utilization of the CUDA implementation of CD from [60], which significantly enhances the CD’s running time. Therefore, our future efforts will be focused on enhancing the running time of SWD to broaden the potential applications of this metric.

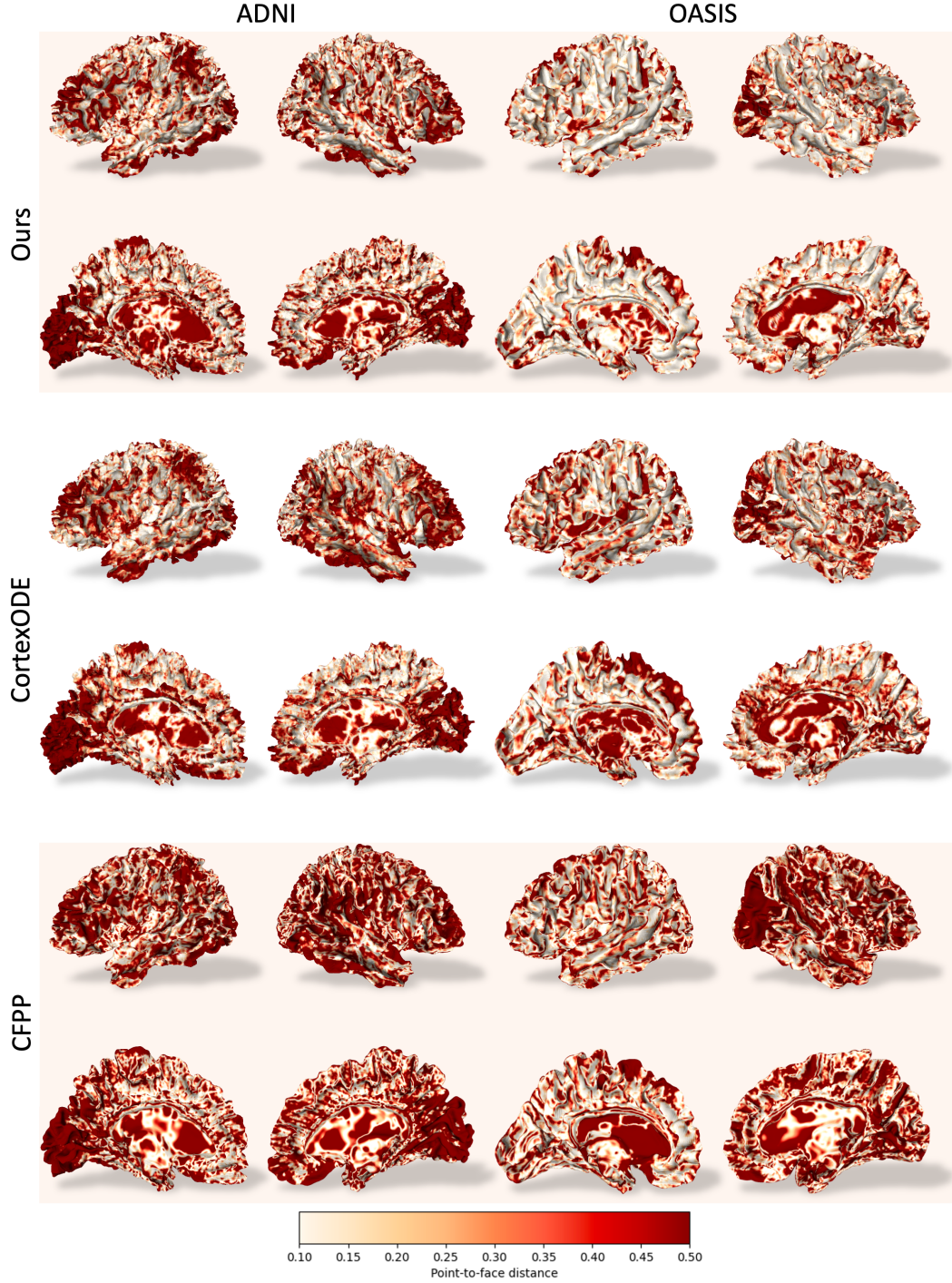


Figure 5: More examples of predicted mesh color-coded with the distance to the ground-truth surfaces as shown in Fig. 3 of the main paper. Each column in the figure corresponds to a randomly selected prediction from our test set.

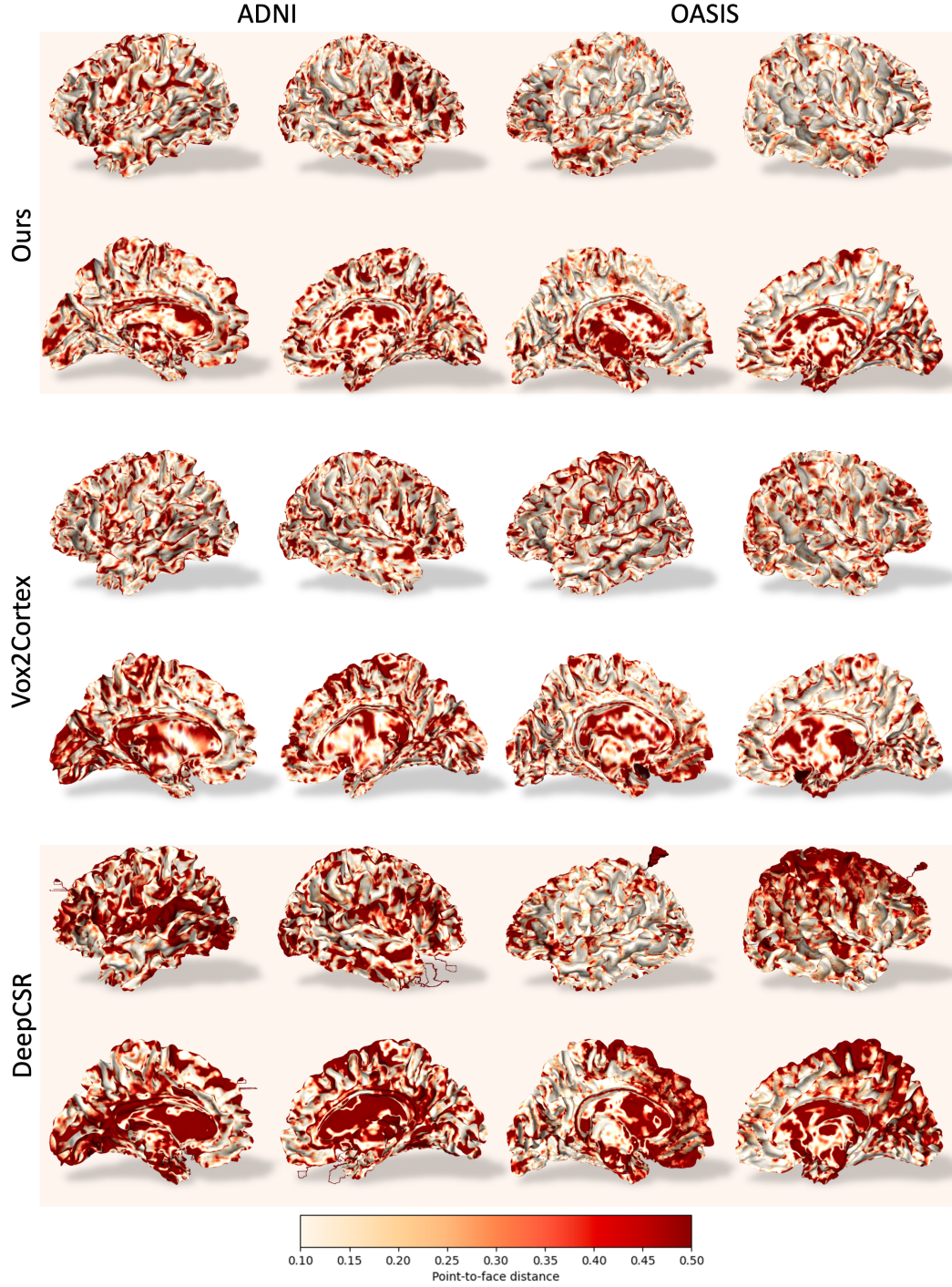


Figure 6: More examples of predicted mesh color-coded with the distance to the ground-truth surfaces as shown in Fig. 3 of the main paper. Each column in the figure corresponds to a randomly selected prediction from our test set.